Physica E 44 (2012) 1780–1786

Contents lists available at SciVerse ScienceDirect

Physica E

journal homepage: www.elsevier.com/locate/physe

# A computational study of ballistic graphene nanoribbon field effect transistors

Maziar Noei, Mahdi Moradinasab *, Morteza Fathipour

*School of Electrical and Computer Engineering, University of Tehran, Tehran, Iran*

ARTICLE INFO

*Article history:*
Received 19 September 2011
Received in revised form
15 December 2011
Accepted 15 December 2011
Available online 28 December 2011

ABSTRACT

A self-consistent solution of Schrödinger equation based on Green's function formalism coupled to a two-dimensional Poisson's equation for treating the electrostatics of the device is used to simulate and model the ballistic performance of an armchair edged GNRFET. Our results take into account interactions of third nearest neighbors, as well as relaxation of carbon–carbon bonds in the edges of nanoribbons. Performance of the *I–V* characteristics of GNRFETs for different widths and lengths is studied in terms of their subthreshold swing, saturation behavior, leakage current and on-current density. This can help in optimizing the fabricated GNRFET devices in terms of their geometrical dimensions as well as their supply voltage and bias point for optimum attainable performance. The impact of channel region's coupling to the source/drain leads is also studied in the last Section of our work.



## 1. Introduction

The International Technology Roadmap for Semiconductors (ITRS) foresees an end-of-life for scaled CMOS technology around 2022 [1]. Indeed CMOS technology is fast reaching the limits of atomic engineering. As a result of Moore's law and ITRS's further requirements, several beyond-CMOS devices have been proposed in the recent years to overcome the scaling limitations that are being experienced in today's CMOS technology. Among these possibilities, Graphene, a monolayer of carbon atoms tightly packed into a hexagonal two-dimensional lattice, is currently being investigated as a possible candidate material for the post-CMOS era. Graphene is compatible with the planar technology particularly high resolution lithography, and shares the same honeycomb lattice structure as Carbon Nanotubes. It provides promising electronic properties such as high carrier mobility and long phase coherence lengths, as well as linear energy dispersion relation at low energies, which results in electronic carriers mimicking the massless and relativistic Dirac particles. This structure has attracted a lot of attention from the condensed matter and device research community in the recent years.

Despite these remarkable properties, graphene sheets are zero-gap materials and result in MOS devices with a very low $I_{on}/I_{off}$ ratio. Therefore, a considerable amount of research effort in the field of graphene has concentrated on attempts to introduce an energy gap in its band structure. In order to do so, a number of procedures have been proposed including gate modulation of bilayer structures [2], chemical functionalization [3] and employing quantum confinement phenomena and edge effects [4]. Among these options, Graphene Nanoribbons (GNRs), which are high-aspect-ratio graphene strips, have shown a great potential to replace the conventional CMOS technology both because of their similarities in electronic and mechanical properties to CNTs, and the promising progress that has been achieved in their fabrication and patterning on planar surfaces [5,6]. Between different directions in which a nanostrip can be patterned on a graphene sheet, the so-called armchair nanoribbons seem to be better choices for semiconductor devices. The armchair arrangement of atoms along the nanoribbon edges opens a bandgap, which in general increases as the ribbon width is decreased [7]. It has been shown that in order to have a reasonable bandgap of about 0.2–0.3 eV, nanoribbons with widths less than 5 nm are required [8].

Recently, the electronic transport in semiconducting nanoribbons of graphene has introduced new areas in nanoelectronics. The unique and impressive electronic properties of GNRs, such as their remarkably high mobility and orientation and width dependence of transport behavior, provide great prospects for their application in electronic devices. An example on applications of GNR is as the channel material for field effect transistors or GNRFETs for short, aimed for high speed switching applications [9]. Theoretical studies indicate that GNRFETs could have a similar performance as CNTFETs and might exceed the conventional Silicon-based FETs [10]. The ultimate destination in this

* Corresponding author. Tel.: +98 21 8208 4334; fax: +98 21 8877 8690.
*E-mail addresses:* m.moradinasab@ece.ut.ac.ir, m.moradinasab@gmail.com (M. Moradinasab).

1386-9477/$ - see front matter © 2011 Elsevier B.V. All rights reserved.
doi:10.1016/j.physe.2011.12.018

promising field is to realize graphene-based nanodevices and all-graphene integrated circuits, which can be fabricated by using the existing planar technologies.

It is pretty obvious that for novel structures of a few nanometers in size, some of the previously unimportant effects such as the number of charge carriers and presence of single dopant atoms or single atom defects, as well as very large surface-to-volume ratio and domination of quantum phenomena can have a significant influence on the overall properties of the structure. In the case of GNRs, their extraordinary electronic properties necessitate theorists to revisit the theoretical basis of contemporary solid state physics in order to analyze the quantum effects that influence the performance and behavior of GNRFETs and other GNR-based devices. There has not been enough time to fully analyze and understand every quantum mechanical aspect that plays a part in electronic properties of these novel structures. Therefore, still many issues about GNRFETs demand more study.

In this paper, we will focus our discussion on the basic electronic and transport properties of GNRFETs. In order to do so, single-electron transport will be described within length scales much shorter than the phase coherence length. We will use the Non-equilibrium Green's Function (NEGF) formalism and a more precise Hamiltonian matrix to calculate the transmission coefficients and the current–voltage characteristics of a typical GNRFET, which is presented in Fig. 1(a). Therefore, the paper is organized as follows. After this introduction (Section 1), in Section 2 we present the formalism and Hamiltonian matrix which is used in our simulations. In Section 3 we look at the electronic transport characteristics of our GNRFET and perform a comprehensive study of the impact of channel region's coupling to the source/drain contacts. Conclusions are finally drawn in Section 4.

## 2. Methodology

Fig. 1(a) shows a honeycomb lattice ribbon with armchair edges attached to two metallic semi-infinite electrodes. A schematic diagram of these contacts is shown in Fig. 1(b), where they are assumed to be square-shaped similar to those used in [11]. In our simulation studies the contact widths is assumed to be 10 times larger than the width of the nanoribbon in channel region. We take the tight-binding parameter of the adjacent atoms in the contact to be equal to the carbon–carbon tight-binding parameter. This gives us a good enough transmission through the

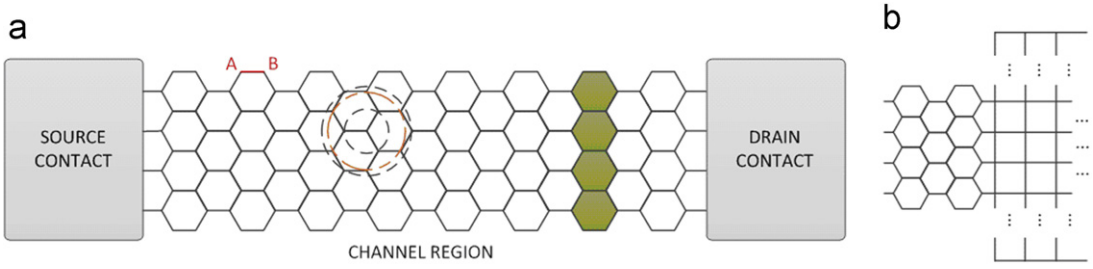


**Fig. 1.** (a) A Schematic sketch of the simulated GNRFET. (b) The contact type used in our simulations.

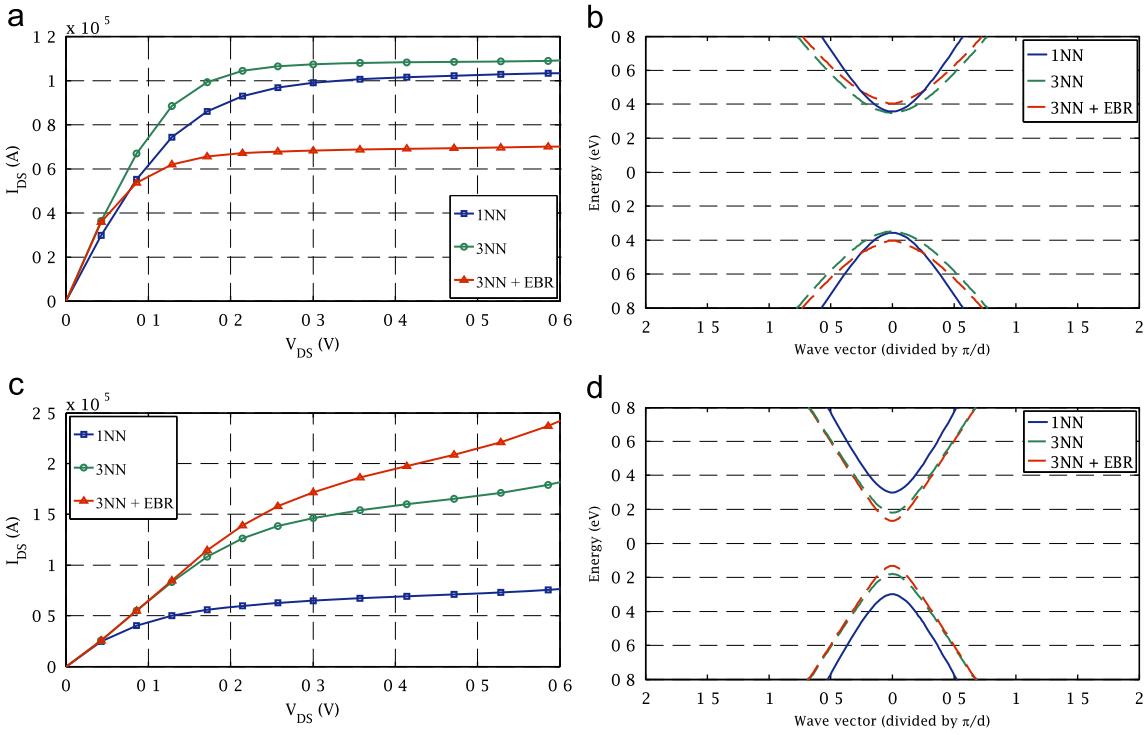


**Fig. 2.** (a) Simulated $I_{DS}$ vs. $V_{DS}$ for a 1.48 nm wide, 15 nm channel long armchair GNR, (b) Band structure of a 1.48 nm wide armchair GNR, (c) Simulated $I_{DS}$ vs. $V_{DS}$ for a 1.72 nm wide, 15 nm channel long armchair GNR and (d) Band structure of a 1.72 nm wide armchair GNR for different modes of accuracy. For all devices $V_{GS}$=0.5 V was assumed.

contact/channel/contact system and allows us to focus our study on the impact of channels nanoribbon on the devices electrical characteristics. The edges of GNR are considered to be passivated by hydrogen. This assumption affects only the $sp_2$ bonding, and has little influence on the QUOTE bonds. We also assume that the structure is relaxed at room temperature. In the following sections, GNRs are labeled based on the number of honeycombs along the width of the nanoribbon. Hence, the nanoribbon demonstrated in Fig. 1 is an $N=4$ armchair GNR. Our Hamiltonian is expressed on a $p_z$ atomic orbital basis set in the real space, using the fitted tight-binding parameters that are obtained by calibration of the energy dispersion relationship of subbands on those obtained from first principle calculations. The carbon–carbon hopping integral inside the device region is found to be $\gamma_1 = -2.66$ eV in [10]. Furthermore, the following effects are taken into account:

(i) *The third nearest neighbors (3NN) in tight-binding calculations:* It has been shown in [9] that by taking the interactions with more distant neighbors into consideration, a qualitative improvement in the tight-binding picture is gained. The second nearest neighbor interaction only shifts the dispersion relation in energy direction. It does not change the bandgap and is not included in our simulations. Therefore, we have used a more precise Hamiltonian matrix based on 1NN and 3NN carbon–carbon interactions. These first and third nearest carbon atoms are shown by black circles in Fig. 1(a). The hopping integral for 3NN interactions is chosen to be $\gamma_2 = -0.3$ eV[12].

(ii) *Effects of edge bond relaxation:* Because each edge carbon atom of a GNR is only bounded to two neighboring atoms, the interatomic distance between A and B sites in Fig. 1(a) will be reduced from 1.42 Å to 1.36 Å when the structure is relaxed to minimum energy. As reported in Refs. [10,13], this edge bond relaxation has a significant influence on the bandgap, effective mass and other qualitative properties of nanoribbons. Therefore, this effect should also be considered in our TB Hamiltonian matrix. Within the TB description, it is common to treat the edge carbon atoms in the same way as the bulk carbon atoms and consider a small perturbation to the edge hopping integral. We consider a change of $\Delta\gamma = -0.2$ eV [12] in nearest neighbor hopping integral for edge carbon atoms to model their relaxation.

(iii) *Potential profile on the channel region:* several works have assumed either a complete potential drop in the channel/contact interface [11] or a linear potential drop in the channel region of a GNRFET [14], both of which are inaccurate assumptions in supply voltages of 0.2 V or more. In this work, the electrostatic potential profile in the device is obtained from a self-consistent solution of the open-boundary Schrodinger equation, which employs NEGF formalism and Poisson's equation using finite difference discretization method in a two-dimensional grid system. By applying finite difference method in our rectangular two-dimensional grid system defined on the GNRFET's channel region, we have discretized Poisson's equation written as

$$AU = -\frac{\Delta^2}{\varepsilon_0 \varepsilon_r}\rho \tag{1}$$

and have solved for the electrostatic potential in the matrix form. Here $U$ and $\rho$ are the electrostatic potential and charge density vectors, respectively, $\Delta$ is the distance between successive grid points and $A$ is a matrix generated from the finite difference method. Boundary conditions for the potential are chosen by the terminal voltages in each bias point [15]. Convergence of the system is achieved when the potential has the required accuracy (0.001 V in our case) in the channel region.

The Hamiltonian matrix can then be written as

$$\mathscr{H}_{ch} = \sum_i \varepsilon_i c_i^\dagger c_i + \sum_i \sum_j \gamma_{ij}(c_i^\dagger c_j + c_i c_j^\dagger) \tag{2}$$

where the operator $c_i^\dagger(c_i)$ creates (annihilates) an electron at site $i$ and the indices $i, j$ are running over all of the atoms in channel region. $\varepsilon_i$ is also the on-site energy for $i$th atom. This term consists of Fermi energy which can simply be set to zero, and the electrostatic potential on $i$ th atom, which is determined by self-consistent solution of Poisson's equation and NEGF equations.

The transmission coefficients in the device region can be expressed in terms of the non-equilibrium Green's function, using the Fisher–Lee relation [16]:

$$T(E) = trace(\Gamma_S G_{ch} \Gamma_D G_{ch}^\dagger) \tag{3}$$

In which we have used the retarded and advanced Green's function for our system, defined by the following expressions:

$$G_{ch} = \{(E+i\eta)I - \mathscr{H}_{ch} - \Sigma_S - \Sigma_D\}^{-1} \tag{4}$$

$$G_{ch}^\dagger = \{(E-i\eta)I - \mathscr{H}_{ch} - \Sigma_S - \Sigma_D\}^{-1} \tag{5}$$

where $\eta$ is an infinitesimal positive number. $\Gamma_S$ and $\Gamma_D$ in (3) are the broadening functions, describing the coupling of device region to the semi-infinite leads [17]. These functions can be calculated by taking the non-Hermitian parts of the so-called self-energy functions, defined as

$$\Sigma_{S/D} = h_{S/D}^\dagger g_{S/D} h_{S/D} \tag{6}$$

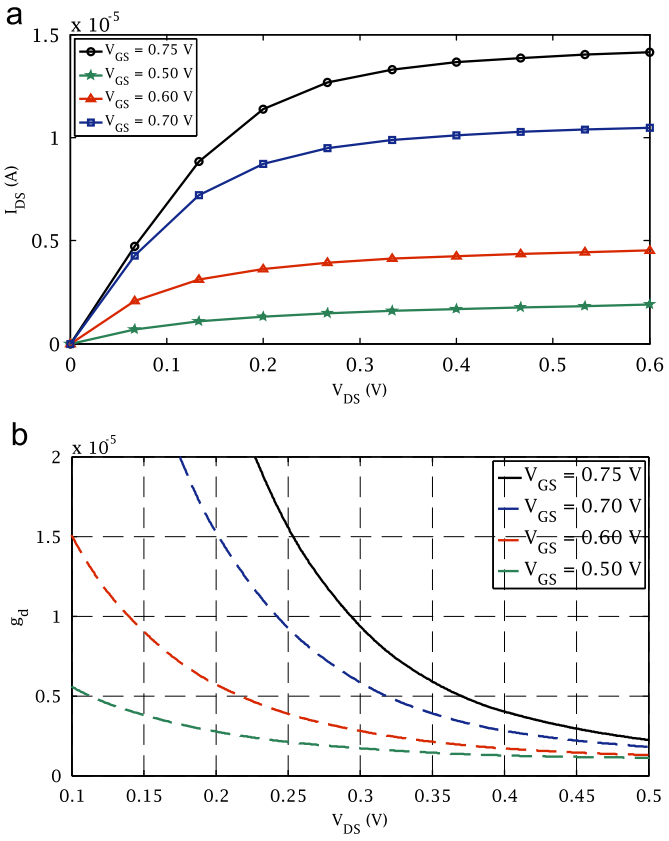


**Fig. 3.** (a) Simulated $I_{DS}$ vs. $V_{DS}$ characteristics and (b) the output conductances for a 1 nm wide and 15 nm channel long armchair GNRFET for different gate biases.

$h_{S/D}$ corresponds to the hopping between channel and source/drain contacts, while $g_{S/D}$ represents the source/drain Green's function. These self-energies can be interpreted as an effective Hamiltonian describing the interaction between device and leads. The contacts' Green's function is of a large size, if not infinite, and in [18,19] algorithms are derived for reducing these functions to finite-sized matrices.

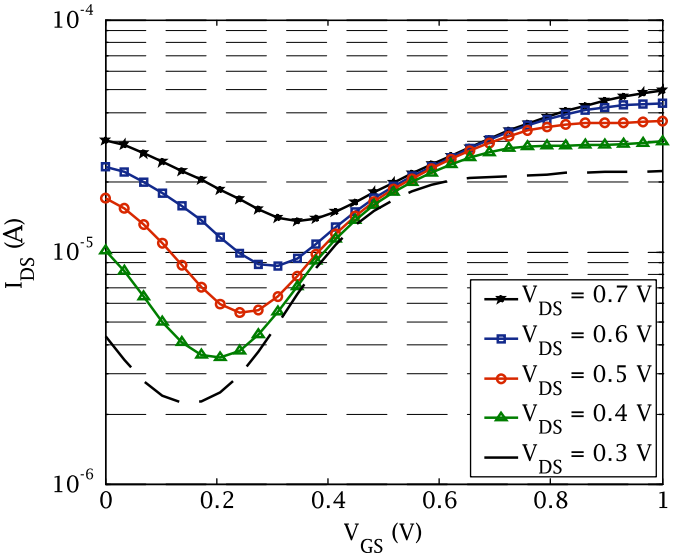


**Fig. 4.** Simulated $I_{DS}$ vs. $V_{GS}$ for a 1 nm wide and 10 nm channel long armchair GNR for different drain to source supply voltages.

The charge density is given by

$$\rho = \frac{1}{2\pi}\int_{-\infty}^{+\infty} dE\left\{f(E,\mu_S)G\Gamma_S G^{\dagger} + f(E,\mu_D)G\Gamma_D G^{\dagger}\right\} \tag{7}$$

With $f(E,\mu_{S/D})$ being the Fermi-Dirac distribution of electrons in the contact at chemical potential $\mu_{S/D}$. Finally, the current passing across the nanoribbon is represented by the area under the graph of $T(E)\{f(E,\mu_S)-f(E,\mu_D)\}$ vs. energy when the self-consistency in all of the previous calculations is achieved. The GNRFET's drain to source current may be calculated as [16]

$$I = \frac{2q}{h}\int_{-\infty}^{+\infty} dE T(E)\{f(E,\mu_S)-f(E,\mu_D)\} \tag{8}$$

## 3. Results and discussion

In order to explore the performance limits of an armchair GNRFET, in this section we perform a series of simulation tests on the structure presented in Fig. 1(a). As mentioned in Section 2, several previous works in this field have neglected the 3NN interactions and relaxation at the edge carbon–carbon bonds. To investigate the validity of this assumption, the output characteristics of the device shown in Fig. 1(a) is presented in Fig. 2 when these two effects are taken into account. The channel material for the GNRFET is a perfectly patterned 15-nm-long armchair nanoribbon. The channel widths are chosen to be 1.48 nm and 1.72 nm, which correspond to 6 and 7 honeycombs in the transverse direction, respectively. $I_{DS}$ vs. $V_{DS}$ is shown for the gate voltage of $V_{GS}$=0.5 V and the results are demonstrated in Fig. 2(a) and (c). These plots show a significant influence of the two previously mentioned effects on the device's performance. For example, by including the third nearest neighbor in the Hamiltonian matrix of a 1.72 nm AGNR, a significant increase in the output current is

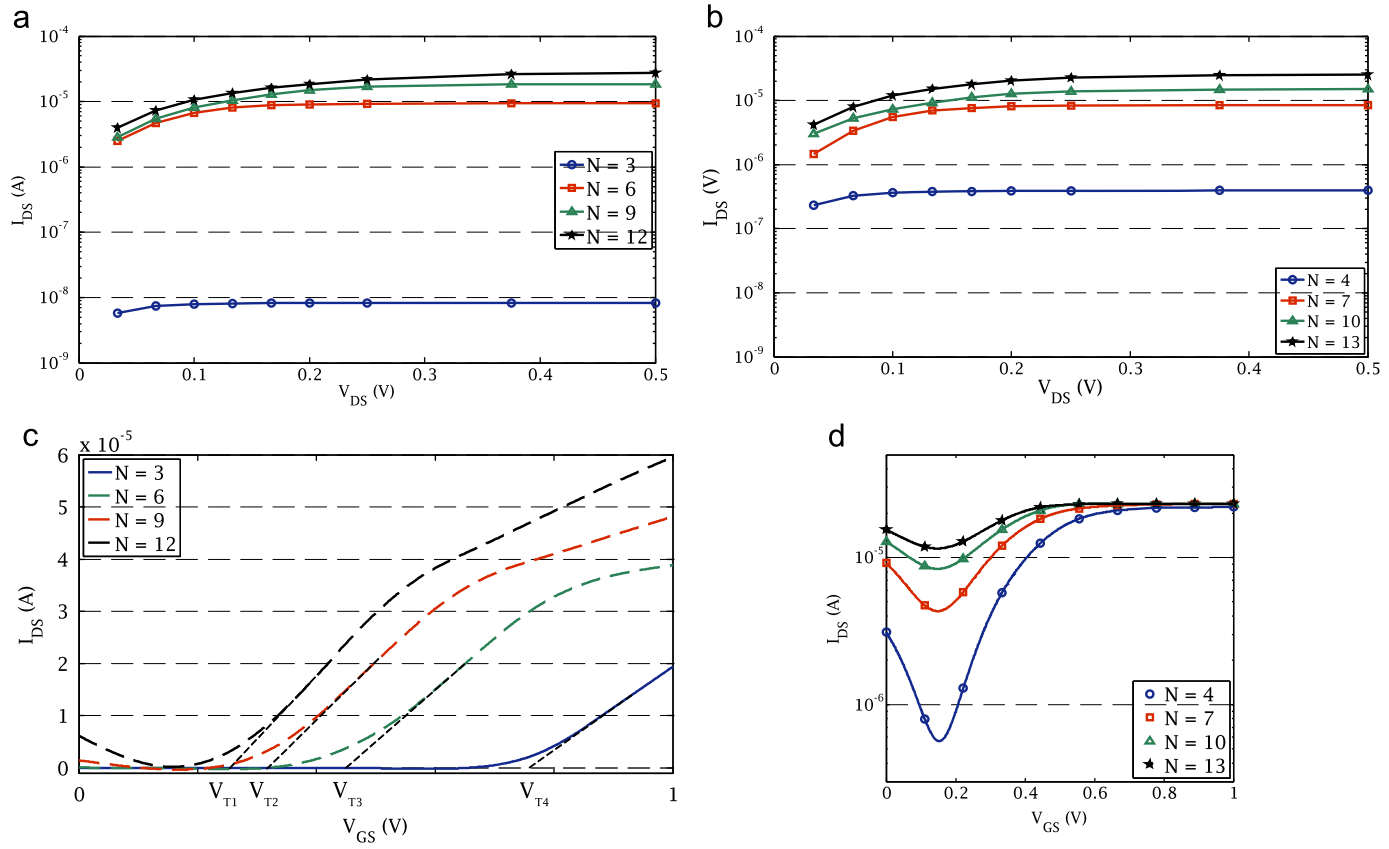


**Fig. 5.** (a,b) Simulated $I_{DS}$ vs. $V_{DS}$ characteristics and (c,d) $I_{DS}$ vs. $V_{GS}$ characteristics of a 15 nm channel long GNRFET for different channel widths.

observed, while considering both 3NN interactions and edge bond relaxation causes even more drastic increase in the output current. It is also observed that under the same bias conditions, considering the 3NN interactions as well as edge bond relaxation may result in different trends for different widths of nanoribbon. To explain these qualitatively different behaviors, we have calculated the band structure of the armchair GNRs with 6 and 7 honeycombs in their width and have plotted the results in Fig. 2(b) and (d). From these plots and other similar results, it can clearly be observed that for nanoribbons with $3p+1$ honeycombs in width (where $p$ is an integer number) the overall effects of edge bond relaxation and 3NN interaction is to decrease the bandgap energy. While, for nanoribbons with $3p$ honeycombs in width, the overall effects of 3NN and edge bond relaxation is opposite, i.e. the bandgap becomes larger. Moreover, these results indicate that considering 3NN and edge bond relaxation has a greater impact on the quantitative results in nanoribbons with $3p+1$ honeycomb width, compared to $3p$ honeycomb width GNRs. $3p+2$ GNRs are not suitable for channel region of a GNRFET due to their very small bandgap. Therefore, they are not included in this work.

We next investigate $I_{DS}$ vs. $V_{DS}$ at different $V_{GS}$ values for a GNRFET with 1 nm channel nanoribbon (corresponding to 4 honeycombs in the width direction). Simulation results are presented in Fig. 3(a). It can be seen that the device demonstrates MOSFET type behavior, and it reaches a current density of approximately 15 mA/μm for $V_{GS}=0.75$ V. This treatment neglects any series resistance or non-ideality that might exist in real devices. Another important parameter to be considered in studying the field effect transistor is its saturation behavior, manifested in the output conductance $g_d$, which is defined as the derivative of the output characteristic with respect to the drain voltage. Fig. 3(b) compares the output conductance for different gate biases. It is shown that when the device is biased at a smaller gate voltage, it shows a better saturation behavior. Thus, there exists an optimum value for the gate bias, which gives sufficient current density as well as a favorable saturation behavior.

The turn-on characteristics for the GNRFET device are reported in Fig. 4 for different $V_{DS}$ values. The channel length is chosen to be approximately 10 nm. In this short-channel regime, band-to-band tunneling mechanism determines a considerable amount of the overall drain-to-source current, where in comparatively longer channels the device's current is nearly completely of thermionic nature. Our formalism can treat both short-channel and quantum tunneling effects and in Fig. 4 it can be seen that by increasing the supply voltage linearly, an exponential increase in the minimal leakage current is resulted. This indicates the significance of proper choice for an optimum value power supply voltage in order to maintain sufficiently small leakage current. It is also obvious from Fig. 4 that higher supply voltages significantly degrade the subthreshold swing. This is attributed to the fact that the gate loses its control on the channel at higher values of drain voltage.

We next study the effect of channel width on the $I$–$V$ characteristics of the device. In order to provide a fair comparison, the nanoribbons of $3p+1$ and $3p$ families were simulated separately and the $I_{DS}$–$V_{DS}$ and $I_{DS}$–$V_{GS}$ characteristics for different channel widths in these families were derived. An armchair edged GNR with larger channel width has a smaller bandgap. This results in a larger on-current, as demonstrated in Fig. 5(a) and (b). However, Fig. 5(d) shows that by increasing the channel width the off-current

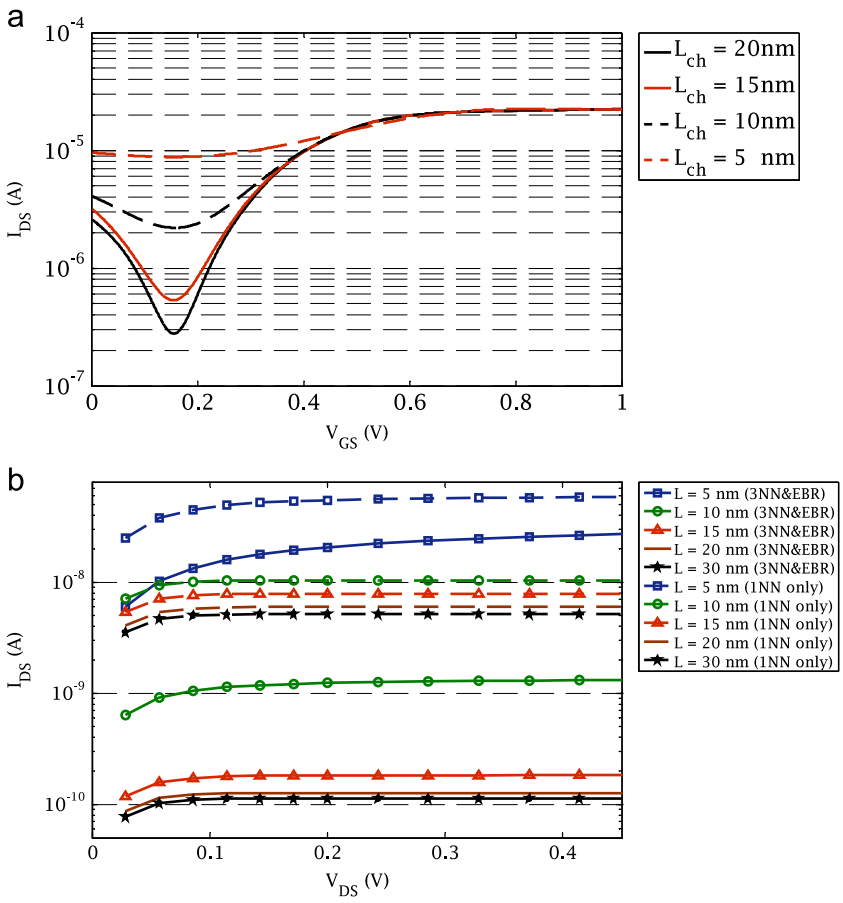


**Fig. 6.** (a) Simulated $I_{DS}$ vs. $V_{GS}$ characteristics and (b) $I_{DS}$ vs. $V_{DS}$ characteristics of a 1 nm channel width GNRFET for different channel lengths. In part (b) the results are plotted for $L=5$ nm (squares), $L=10$ nm (circles), $L=15$ nm (triangles), $L=20$ nm (no sign) and $L=30$ nm (stars). The solid curves consider 3NN and EBR, while in the dashed curves these effects are neglected.

increases as well. This results in a significant degradation in switching performance of the GNRFET. It is clear from Fig. 5(d) that there is also an optimum width for a GNRFET's channel material that gives the highest attainable on-current to off-current ratio $I_{on}/I_{off}$. Fig. 5(c) compares the threshold voltages for GNRFETs with different channel widths. Threshold voltages of the devices are extracted by the linear extrapolation of the drain current curve at the point of maximum slope and are shown in Fig. 5(c). It is observed that by increasing the width of the channel's nanoribbon, the threshold voltage of fabricated device reduces. This too can be attributed to the reduction in nanoribbon's bandgap. In practice, the difference in threshold voltage of different transistors can be controlled by various techniques, such as adjustment of gate work function.

In Fig. 6 the effect of channel length on the $I$–$V$ characteristics of the device is explored. Here, devices with 4 honeycombs in their width direction are simulated in different channel lengths. Fig. 6(a) shows the $I_{DS}$–$V_{GS}$ curves for these GNRFETs, while Fig. 6(b) demonstrates the $I_{DS}$ vs. $V_{DS}$ characteristics for them. The recursive calculations stated in the methodology for obtaining the contacts' self-energies and electrostatics of device are time-consuming. The computational cost increases significantly when the length of the channel is increased and for channel lengths of 15 nm to 20 nm, where the Hamiltonians are becoming larger than $1000 \times 1000$ in size, it takes a long time to obtain the output current for certain gate and drain biases. Since we were interested in the qualitative behavior of the GNRFET when the channel's length is varied, we simulated the $I_{DS}$–$V_{GS}$ for a few number of gate biases, and then performed curve fitting to obtain the approximate curves for $I_{DS}$–$V_{GS}$ characteristics. The obtained results show the dominance of direct band-to-band tunneling and short-channel effects on the current in channels of a few nanometers length, which are suppressed in longer channels. These short-channel phenomena also manifest themselves in the off-currents seen in Fig. 6(a). It can be seen that for long enough channels, further increasing the channel length hardly changes the on-current of the device. This result is different from which we observe in conventional MOSFETs, and can be explained by the fact that we have simulated our device in the ballistic regime and the scattering mechanisms that cause the channel resistance to increase proportional to channel length are neglected here. This is somehow an acceptable assumption and in fact there have been reports of experimental graphene-based devices that operate close to the ballistic limit.

Finally, we investigate the impact of weak channel to source/drain coupling in our device. Here, we have obtained the saturation current and subthreshold swing of several devices with different tight-binding parameters of $\tau_{S/D}$ in $h_{S/D}$ matrices. These parameters represent the hopping strength of the channel's nanoribbon to the contacts. In order to fairly compare the subthreshold swing in different $I_{DS}$ vs. $V_{GS}$ characteristics, we have defined the OFF-state as the gate voltage in which $I_{DS}=10^{-7}$ A and the ON-state is considered to be where the current increases by one order of magnitude. The results are demonstrated in Fig. 7(a). It is observed that the saturation current and subthreshold swing both show an obvious deterioration when the coupling TB parameter between ribbon and contacts is changed from its optimum value of approximately $-2.7$ eV, which is close to the carbon–carbon nearest neighbor integral in the channel region. These results are somehow expected for $\tau_{S/D} > -2.7$ eV (or weak coupling of channel's left/right atoms to source/drain atoms), because in this case the channel/contact bonds act like a potential barrier for some of the low-energy electrons that are present in the channel region. To demonstrate this better, we have presented the transmission probability as a function of energy for different values of $\tau_{S/D}$ in Fig. 7(b). This figure shows that for weak channel-contact coupling, the transmission function exhibits resonant sharp peaks in certain energies, which are not necessarily the resonant energies of the ideal device. These sharp resonances can

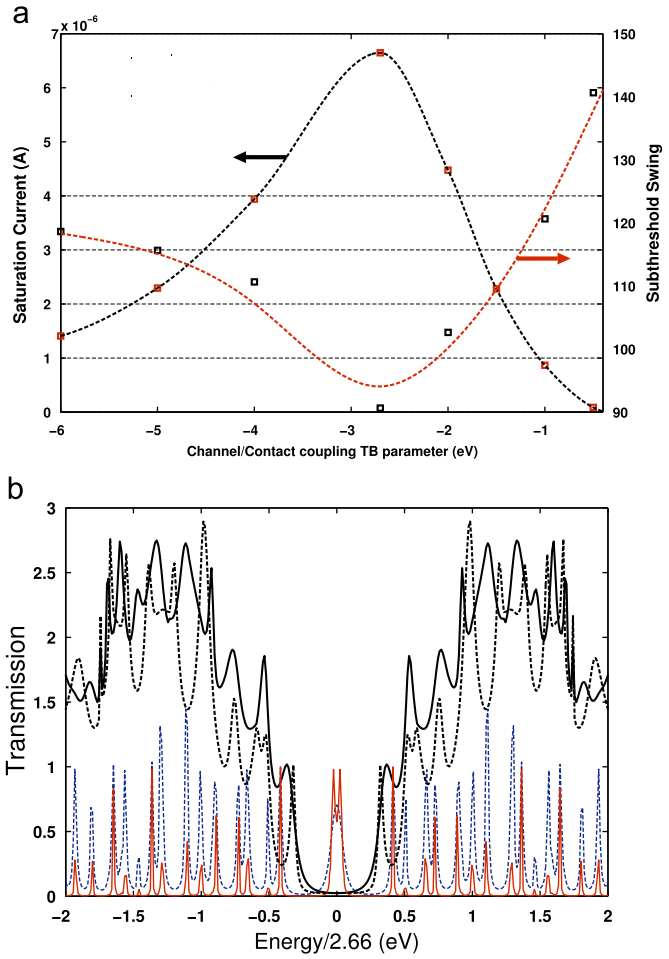


**Fig. 7.** (a) The saturation current and subthreshold swing of a GNRFET as a function of channel/contact coupling TB parameter. (b) The transmission functions vs. energy for different channel/contact coupling TB parameters. The black solid curve corresponds to TB parameter of $-2.7$ eV, while the black dashed curve corresponds to TB parameters of $-5$ eV. The red (gray) solid curve and blue (gray) dashed curve show the transmission for the TB parameters of $-0.5$ eV and $-1$ eV respectively.

be explained by noting that the two channel-contact interfaces act like two potential barriers and create discrete energy levels in the channel region. The transmission probability from source to drain peaks whenever the energy matches one of these levels. For the case of $\tau_{S/D} < -2.7$ eV the channel itself acts as a potential barrier for electrons in the source-channel interface to be injected towards the drain contact. Therefore, a good control on the channel-contact coupling is necessary in designing graphene-based high-performance circuits.

## 4. Conclusion

In presented paper, we studied the $I$–$V$ characteristics of a GNRFET for different operating bias points, as well as different channel lengths and channel widths. In order to improve our results quantitatively, we took the third nearest neighbor interactions and the impact of carbon–carbon bonds' relaxation in nanoribbon's edges into consideration in our tight-binding description of the device. We showed an armchair edged GNRFET's general behavior as a function of different design parameters. Our results clearly demonstrated that there are certain trade-offs in designing a graphene-based low-power or high-frequency circuit and careful optimization of both

topological parameters and operating bias point are necessary. Furthermore, the impact of channel-to-contact coupling on the device's overall performance was explored and it was shown that poor control on the channel-to-contact interface can result in a significant deterioration in the expected performance of a GNRFET.

## References


[1] International Technology Roadmap for Semiconductors 2009, 〈http://www.itrs.net/〉.
[2] H. Min, B. Sahu, S.K. Banerjee, A.H. MacDonald, Physical Review B 75 (April) (2007) 15511521.
[3] D.W. Boukhvalov, M.I. Katsnelson, Physical Review B 78 (Aug) (2008) 0854138.
[4] Y. Son, M.L. Cohen, S.G. Louie, Physical Review Letters 97 (Nov) (2006) 2168037.
[5] B. Huang, Q. Yan, Z. Li, W. Duan, Frontiers of Physics in China 4 (3) (2009) 269279.
[6] Z. Chen, Y.M. Lin, M.J. Rooks, P. Avouris, Physica E: Low–dimensional Systems and Nanostructures 40/2 (2007) 228232.
[7] M.Y. Han, B. zyilmaz, Y. Zhang, P. Kim, Physical Review Letters 98 (May) (2007) 2068059.
[8] G. Liang, N. Neophytou, D.E. Nikonov, M.S. Lundstrom, IEEE Transactions on Electron Devices 54 (4) (2007) 677–682.
[9] S. Reich, J. Maultzsch, C. Thomsen, Physical Review B 66 (Jul) (2002) 0354127.
[10] Z.F. Wang, Q. Li, H. Zheng, H. Ren, H. Su, Q.W. Shi, Jie Chen, Physical Review B 75 (Mar) (2007) 11340610.
[11] R. Moradian, P. Zereshki, S. Haseli, M. Hayati, Physica E 41 (2009) 801805.
[12] Z. Liu-Jun, X. Tong-Sheng, Chinese Physics B 19 (Nov) (2010) 11710512.
[13] O. Hod, J.E. Peralta, G.E. Scuseria, Physical Review B 76 (Dec) (2007) 2334015.
[14] S.K. Maiti, Solid State Communications 149 (25–26) (2009) 973–977.
[15] D.I. Odili, Y. Wu, P.A. Childs, D.C. Herbert, Journal of Applied Physics 106 (2009) 024509.
[16] D.S. Fisher, P.A. Lee, Physical Review B 23 (Jun) (1981) 68514.
[17] S. Datta, Superlattices and Microstructures 28 (4) (2000) 253–278.
[18] P.A. Khomyakov, G. Brocks, V. Karpan, M. Zwierzycki, P.J. Kelly, Physical Review B 72 (Jul) (2005) 03545063.
[19] M.P. Lopez Sancho, J.M. Lopez Sancho, J. Rubio, Journal of Physics F: Metal Physics 14 (May) (1984) 120515.